

# A journey to ITACA

## Ion Tracking with Ammonium Cations Apparatus

J. J. Gómez-Cadenas<sup>a,1,2</sup>, L. Arazi<sup>3</sup>, M. Elorza<sup>1,4</sup>, Z. Freixa<sup>4,2</sup>,  
F. Monrabal<sup>1,2</sup>, A. Pazos<sup>4</sup>, J. Renner<sup>5</sup>, S.R. Soleti<sup>b,1,2</sup>, S. Torelli<sup>1</sup>

<sup>1</sup>Donostia International Physics Center, San Sebastián / Donostia, E-20018, Spain

<sup>2</sup>Ikerbasque (Basque Foundation for Science), Bilbao, E-48009, Spain

<sup>3</sup>Ben-Gurion University of the Negev, Beer-Sheva, 8410501, Israel

<sup>4</sup>Universidad del País Vasco (UPV/EHU), San Sebastián / Donostia, E-20018, Spain

<sup>5</sup>Instituto de Física Corpuscular (IFIC), Paterna, E-46980, Spain

Received: date / Accepted: date

**Abstract** A unique feature of gas xenon electroluminescent time projection chambers (GXeEL TPCs) in  $\beta\beta 0\nu$  searches is their ability to reconstruct event topology, in particular to distinguish “single-electron” from “double-electron” tracks, the latter being the signature of a  $\beta\beta 0\nu$  decay near the decay endpoint  $Q_{\beta\beta}$ . Together with excellent energy resolution and the  $t_0$  provided by primary scintillation, this topological information is key to suppressing backgrounds. Preserving EL, however, requires operation in pure xenon (with helium as the only benign additive), where electron diffusion is large. Consequently, reconstructed track fidelity is limited by diffusion and intrinsic EL blurring.

We propose augmenting the detector with the ability to image not only the electron track but also the corresponding mirror ion track. Introducing trace amounts of  $\text{NH}_3$  ( $\sim 100$  ppb) converts primary xenon ions into ammonium ions,  $\text{NH}_4^+$ , via a fast two-step ion–molecule process involving charge transfer followed by proton transfer, while leaving EL unaffected. Electrons drift rapidly to the anode, producing the standard EL image, whereas  $\text{NH}_4^+$  ions drift slowly toward the cathode, allowing time to determine the event energy and barycenter. For events in the region of interest, an ion sensor near the cathode at the projected barycenter captures the ions. Laser interrogation of the sensor’s molecular layer then reveals an ion-track image with sub-millimeter diffusion and no EL-induced smearing.

Combined electron–ion imaging strengthens topological discrimination, improving background rejection by about an order of magnitude and significantly extending the discovery potential of GXeEL TPCs for very long  $\beta\beta 0\nu$  lifetimes.

<sup>a</sup>e-mail: jggomezcadenas@dipc.org

<sup>b</sup>e-mail: roberto.soleti@dipc.org

**Keywords** Neutrinoless double beta decay · TPC · high-pressure xenon chambers · Xenon

### 1 Introduction

The observation of neutrinoless double-beta decay ( $\beta\beta 0\nu$ ) would demonstrate that the neutrino is a Majorana particle, establish lepton-number violation, and shed light on the absolute neutrino mass scale [1–3]. Detecting this rare process requires ultra-low background experiments with large isotopic masses and excellent energy resolution to resolve a possible signal peak at the decay Q-value ( $Q_{\beta\beta}$ ) from background events.

The present generation of experiments has pushed the  $\beta\beta 0\nu$  sensitivity to half-lives beyond  $10^{26}$  years, with the most stringent limit set by KamLAND-Zen at  $T_{1/2} > 3.8 \times 10^{26}$  yr for  $^{136}\text{Xe}$  [4]. Other leading efforts include the LEGEND experiment, which has set a limit of  $T_{1/2} > 1.9 \times 10^{26}$  yr for  $^{76}\text{Ge}$  [5]. The goal of next-generation experiments, being currently planned is to reach a sensitivity of  $T_{1/2} > 10^{27}$  yr, and, ultimately,  $T_{1/2} > 10^{28}$  yr.

Over the last decade and a half, the technology of high pressure gas TPCs, operating with xenon and using electroluminescent amplification (GXeEL) has been developed by the NEXT collaboration, evolving it from early prototypes [6–11] to a 100 kg-scale apparatus (NEXT-100) [12], currently searching for neutrinoless double beta decay processes ( $\beta\beta 0\nu$ ) in  $^{136}\text{Xe}$  at the Canfranc Underground Laboratory. The large NEXT-100 detector achieves an excellent energy resolution of  $(0.93 \pm 0.02)\%$  FWHM at  $Q_{\beta\beta}$  [13], while the AXEL collaboration obtains  $(0.67 \pm 0.08)\%$  in a mid-sized prototype [14].

A GXeEL TPC provides a distinctive topological signature that enables identification of events with two emitted electrons. A  $\beta\beta 0\nu$  candidate in the apparatus is defined as a single, continuous track (with no detached energy deposits), reconstructed with total energy within the region of interest (ROI) around  $Q_{\beta\beta}$  and fully contained inside the fiducial volume, away from detector surfaces. This “single-track” requirement suppresses nearly all radioactive backgrounds, leaving only single-electron events with energies near  $Q_{\beta\beta}$ , such as those arising from photoelectric interactions of the 2.446 MeV  $\gamma$  line of  $^{214}\text{Bi}$  and the 2.615 MeV line of  $^{208}\text{Tl}$ . The effectiveness of this topological discrimination has been demonstrated by the NEXT collaboration [15].

However, the performance of the topological signature in a GXeEL TPC is limited by the use of pure xenon and by electroluminescent (EL) amplification. As ionization electrons drift through the dense gas, they undergo diffusion, producing a charge cloud whose transverse size increases with the drift length. In addition, EL amplification introduces further blurring, as the EL photons are emitted isotropically.

The NEXT collaboration has extensively investigated methods to reduce electron diffusion in xenon gas. One of the most effective proposed approaches is the use of Xe/He mixtures (typically 85/15%) [16–18], which may reduce the transverse diffusion coefficient by about a factor 2. Other additives such as  $\text{CH}_4$  and  $\text{CO}_2$  have also been studied [19, 20]. These gases cool the drifting electrons efficiently but strongly quench xenon scintillation, creating a trade-off between reduced diffusion and loss of electroluminescent (EL) yield.

Here we propose a new concept to measure event topology in an GXe TPC, which we assumed EL, given that  $t_0$  is needed and excellent energy resolution is a bonus. The method relies on recording two complementary tracks for each event: the *electron track* ( $eT$ ), the established signature in a GXe TPC, and an *ion track* ( $iT$ ), formed by suitable positive ions that can be trapped by a molecular layer of sensors similar to those developed by the NEXT collaboration in the context of their “barium tagging” program [21–29]. It is worth noting that related concepts based on negative ion drift, originally developed by the DRIFT collaboration for directional dark matter searches to strongly suppress diffusion, have been explored previously and demonstrated experimentally, albeit in a different physics context [30, 31]. More recently, similar ideas have been revisited and extended in the context of combined ion–electron imaging [32]. We call this concept ITACA (Ion Tracking with Ammonium Cations Apparatus).

This paper is organized as follows: section 2 reviews the reconstruction of the event topology in a GXeEL TPC. Section 3 proposes a conceptual design for the ITACA detector. The principle of operation is examined in 4. In section 5 we describe the ion track detector and in section 6 we briefly discuss the potential enhancement in sensitivity provided by the ITACA technique. We present our conclusions in 7.

## 2 Reconstruction of event topology in a GXeEL TPC

A GXeEL TPC operates as shown in Figure 1. Xenon emits UV scintillation at 172 nm due to excimer formation and decay, marking the event start,  $t_0$ . A moderate electric field (a few hundred V/cm) transports ionization electrons to the TPC anode, crossing a higher electric field (EL) region. Here, electrons excite xenon atoms without further ionization, causing a proportional burst of secondary scintillation light. This amplification, with sub-poissonian fluctuations ensures excellent energy resolution by consistently collecting almost all ionization charge.

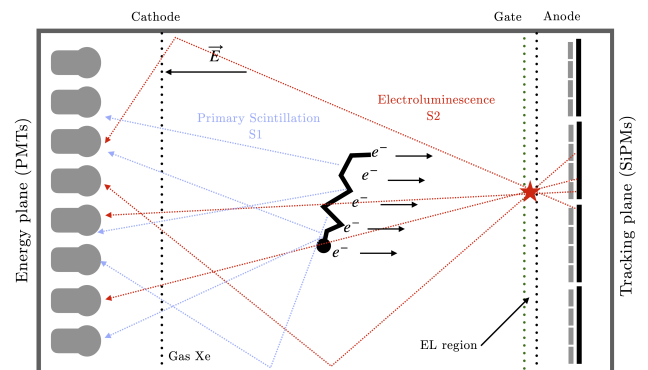


**Fig. 1** Principle of operation of of an asymmetric GXeEL TPC with SiPMs and PMTs.

The EL region is defined by two transparent grids separated by a small gap (about 5-10 mm): the anode, held at ground potential, and the gate, biased to produce a reduced electric field of roughly 2 kV/cm/bar. Under typical conditions, about  $10^3$  photons are emitted per ionization electron. Photons directed toward the anode are detected in a pixelated detector. All the NEXT detectors, as well as the AXEL prototypes use an array of silicon photomultipliers (SiPMs) with a typical pitch of 10 mm. Event tracks are reconstructed by combining the spatial information from the SiPMs with the timing provided by the TPC. In an asymmetric TPC, such as the NEXT-100 detector and the AXEL

prototype, photons emitted toward the cathode are recorded by photomultipliers located behind the transparent cathode, which also detect the primary scintillation signal (S1). The decay  $^{136}\text{Xe} \rightarrow ^{136}\text{Ba}^{2+} + 2e^-$  releases  $Q_{\beta\beta} = 2.458$  MeV, and thus  $1.1 \times 10^5$  electron pairs, distributed along a twisted trajectory of about 10-15 cm path length when operating at pressures around 15 bar.

Figure 2 displays the ionization pattern from two electrons generated in a simulated  $\beta\beta 0\nu$  event. Multiple scattering bends their paths, which end in dense “blobs” of energy deposition at the Bragg peaks.

**Table 1** Measured longitudinal ( $D_L$ ) and transverse ( $D_T$ ) diffusion coefficients for pure xenon and 10% Xe/He gas mixtures, expressed in  $\sqrt{\text{bar mm}/\sqrt{\text{cm}}}$ .

Gas mixture	$D_L$ ( $\sqrt{\text{bar mm}/\sqrt{\text{cm}}}$ )	$D_T$ ( $\sqrt{\text{bar mm}/\sqrt{\text{cm}}}$ )
Pure Xe	0.900	3.500
Xe + 10% He	0.750	1.600

The reconstruction of topology in a GXeEL TPC is influenced by two distinct smearing effects. The first arises from the spatial spread of electroluminescent (EL) light as electrons are accelerated in the EL region. This effect can be accurately modeled by a Gaussian distribution and precisely characterized using calibration data [33, 34]. The second, and more significant, contribution comes from the longitudinal and transverse diffusion of drifting electrons, which can be expressed as:

$$\sigma_{l,t}(\text{mm}) = \frac{D_{l,t}}{\sqrt{P}} \times \sqrt{L} \quad (1)$$

where, if  $L$  is expressed in cm and  $P$  in bar,  $D_{l,t}$  is expressed in  $\sqrt{\text{bar mm}/\sqrt{\text{cm}}}$ .

Table 1 shows the values of  $D_{l,t}$  for pure Xenon and for a 0.9/0.1 mixture of Xenon and Helium, which substantially reduces the transverse diffusion [16, 18, 19].

Figure 3 shows the reconstruction of the XY projection of the event displayed in Figure 2 for the case of pure xenon and for a 0.9/0.1 Xe/He mixture. Three representative drifting distances are considered. Notice that the smearing of the tracks near the cathode is very large, even with Xe/He mixture. As the impact of the diffusion is reduced, the details of the track becomes sharper, ultimately revealing the two blobs (as well as any potential energy deposit near the track, such as for example the characteristic 30 keV X-ray in the photoelectric interaction of the 2448 MeV  $\gamma$  produced in  $^{214}\text{Bi}$  decays) with great detail.

To separate signal and background events in the search for  $\beta\beta 0\nu$  decays, a GXe TPC exploits the different topology of the two electrons emitted in a double beta decay, and the single electrons (often accompanied by additional energy depositions) which constitute the main backgrounds. The three main sources of background are: the  $\gamma$  line of 2447 keV arising from  $^{214}\text{Bi}$  decays, ( $\gamma_{214\text{Bi}}$ ); the  $\gamma$  line of 2615 keV arising from  $^{208}\text{Tl}$  decays ( $\gamma_{208\text{Tl}}$ ), and the single electrons from the  $^{137}\text{Xe}$   $\beta$  decay with energies compatible with the region-of-interest (ROI) of the  $\beta\beta 0\nu$  search (typically 1 FWHM around  $Q_{\beta\beta}$ ). Given that the ROI width for EL detectors is of the order of 15-25 keV, while the distance between  $Q_{\beta\beta}$  and the  $\gamma_{214\text{Bi}}$  photopeak is 10 keV, topology becomes specially important to suppress this background source, but is also needed to reduce the flat background from  $^{137}\text{Xe}$  decays and Compton interactions of the  $\gamma_{208\text{Tl}}$ .

The  $\gamma_{214\text{Bi}}$  photopeak produces a single electron, accompanied 85% of the times by the characteristic de-excitation X-ray of xenon (with an energy of about 30 keV), and occasionally Bremsstrahlung emission. The  $\gamma_{208\text{Tl}}$  introduces background in the ROI via Compton electrons, which come together with the scattered Compton photon and eventually Bremsstrahlung. The  $^{137}\text{Xe}$   $\beta$  decay produces a single electron, with end point energy of 4.17 MeV, thus intersecting the ROI. Also this electron can emit Bremsstrahlung. In all cases, therefore, imposing a single track with no extra energy deposition is advantageous to separate signal from backgrounds. The second requirement is to be able to separate the signature of one electron from that of two electrons. Thus, the signature of the double beta decay is a single connected track with two energy blobs of similar intensity in each of the track extremes, as those that can be observed in Figure 3.

Reducing diffusion has two positive effects. On one side, it permits a better separation between deposits (such as the 30 keV X-ray signaling a  $\gamma_{214\text{Bi}}$  photoelectric interaction) and the main electron track. On the other, it allows resolving better the two blobs of a signal event.

### 3 The ITACA Detector

The ITACA (Ion Tracking with Ammonium Cations Apparatus) concept is shown in Figure 4. Trace amounts (100 pb) of ammonia ( $\text{NH}_3$ ) are added to the gas (assumed to be a 0.9/0.1 Xe/He mixture<sup>1</sup>). In spite

<sup>1</sup>So far, all GXeEL TPCs have operated with pure xenon, although the NEXT collaboration aims to use eventually Xe/He mixtures [35].

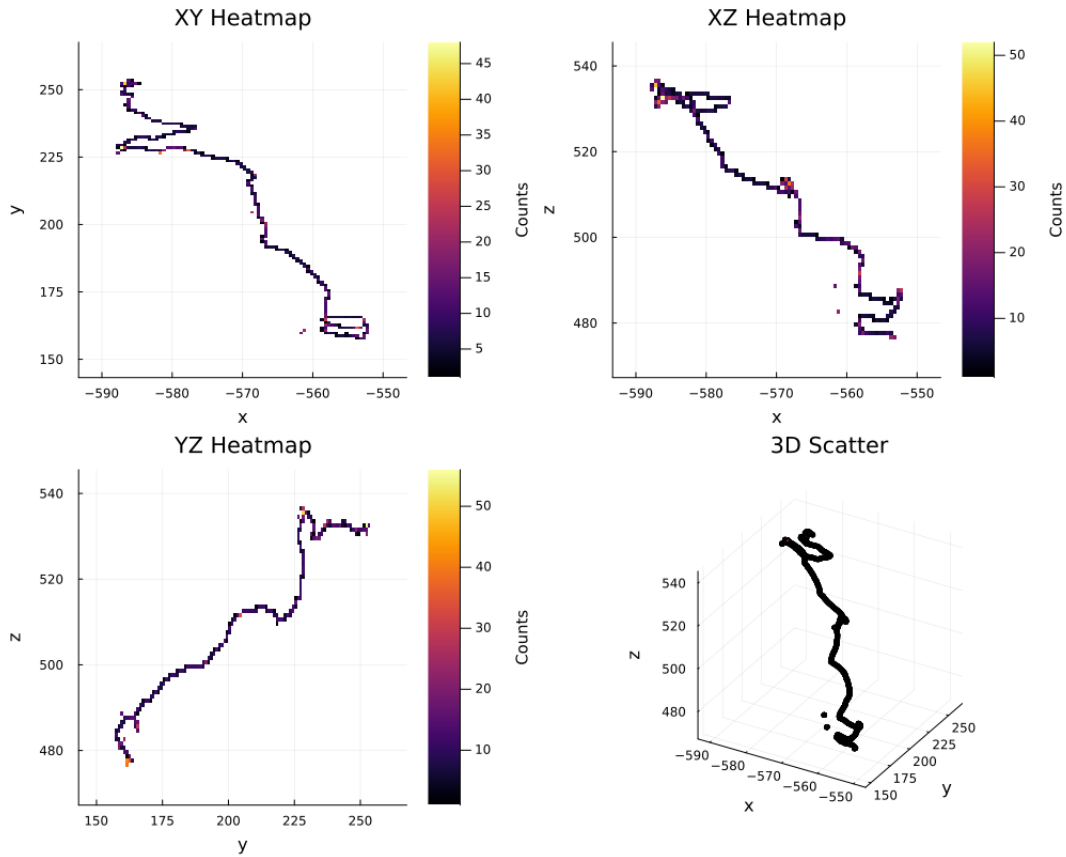


**Fig. 2** A simulated  $\beta\beta\nu$  track in HPXe.

of the low concentration, this is enough to transform positive xenon ions into ammonium ( $\text{NH}_4^+$ ), without quenching the EL light or affecting the electron drift.

Positive  $\text{NH}_4^+$  ions, then, drift to the cathode, in a time scale of seconds, while the electrons drift to the anode three orders of magnitude faster. Ion diffusion is much smaller than electron diffusion, and thus, reconstruction of the ion track (iT), combined with the electron track (eT) improves the topological rejection of backgrounds. This is enhanced by the fact that the diffusion in the ion and electron tracks is anticorrelated, as illustrated in Figure 5. Consider two extreme cases. When electrons are near the anode (10 cm) diffusion is small, and the reconstructed track can be combined with the ion track. Instead, when electrons are far from the anode (100 cm) the reconstructed electron track is totally blurred, but the ion track is reconstructed with very small diffusion, and the resulting track resolves the blobs in exquisite detail. The availability of the ion track, thus, allows a uniform topological reconstruction across the detector.

For definiteness, let us consider an implementation of the ITACA concept able to hold 1 tonne of xenon at high pressure, with the following parameters:

1. TPC diameter: 200 cm.
2. TPC length : 200 cm.
3. Operating pressure: 30 bar.
4. Mass of xenon: 1.2 ton.
5. Density:  $n_{\text{Xe}} = 9 \times 10^{20}$  atoms/cm<sup>3</sup>.
6. Drift field: 400 V/cm.

ITACA is an asymmetric EL TPC, like NEXT-100, but instrumented like the proposed NEXT-HD detector [35]: it deploys a fiber barrel calorimeter [36], able to measure the primary scintillation S1 (and thus the start-of-the-event  $t_0$ ) as well as the EL light S2, and a Dense Silicon Plane, able to measure S2 and to reconstruct the electron track.

Operation at higher pressure results in shorter electron tracks (w.r.t. NEXT-100 and NEXT-HD), but also smaller diffusion (a factor  $\sqrt{2}$  less than NEXT-100 and NEXT-HD). Electron drift velocity is of the order of 100 cm/ms, while ion drift velocity is of the order of 25 cm/s, as we will discuss below. Operation of ITACA at this high pressure has the advantage of allowing a more compact detector and permits a longer fiducial region.

This last point deserves some discussion. To define the fiducial region in  $z$ , we need to assess what is the minimum distance between the barycenter of a  $\beta\beta\nu$

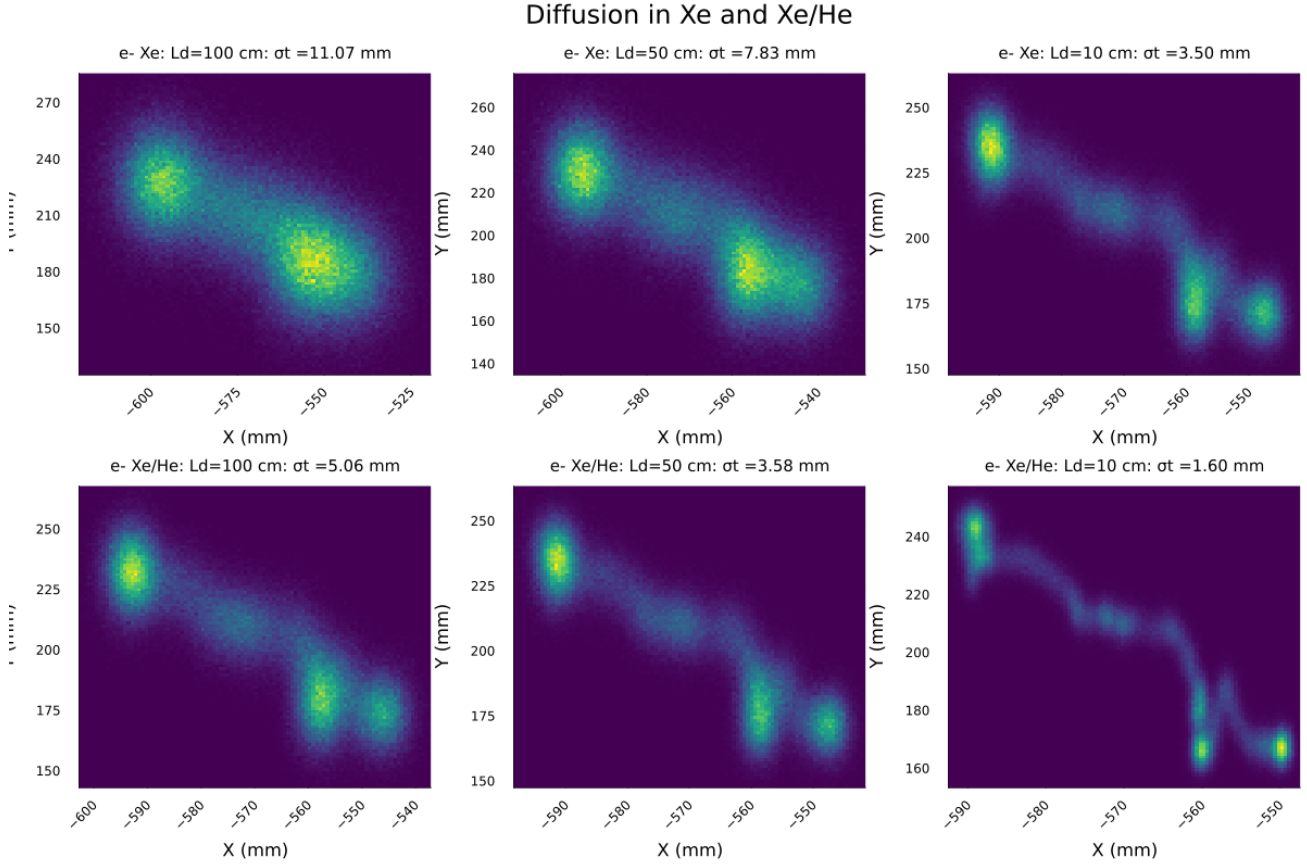


**Fig. 3** Reconstruction of a  $\beta\beta\nu$  track a GXeEL TPC with 1 m electron drift. The upper row shows the XY projection of the track in pure xenon, for the characteristic distances. Near the cathode ( $\sim 100$  cm) in the middle of the drift ( $\sim 50$  cm) and near the anode ( $\sim 10$  cm). The bottom row shows the same projections for Xe/He.

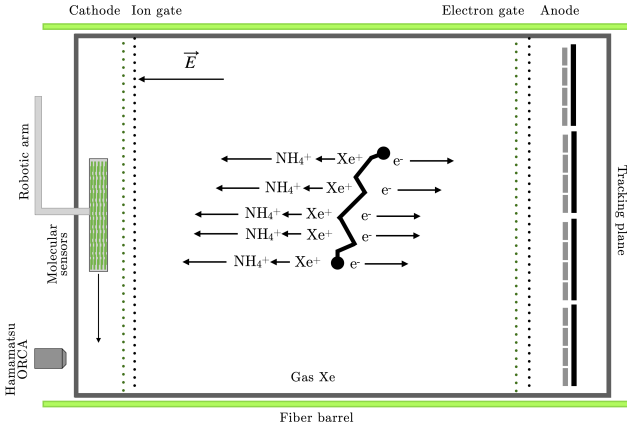


**Fig. 4** Principle of operation of ITACA.

decay candidate and the anode that allows the reconstruction of the ion track. We allow a minimum delay time of  $t_d \sim t_0 + 500$  ms, which is needed to: a) compute the energy of the event; b) reconstruct the event rough topology and compute its barycenter,  $P$ ; c) compute the projected position of the barycenter,  $P'$  in the anode detection plane; d) move the so-called Molecular

Ion Detector, defined in section 5, to  $P'$ , so that it can capture the incoming ion track.

On the other hand, the ion drift velocity is 20 cm/s, thus allowing 10 cm minimum drift is sufficient to grant  $t_d > 500$  ms. The fiducial region is thus 190 cm, and only 5% of the fiducial volume in  $z$  is lost.

Ion collection is performed through a gated scheme, in which the ion detector is exposed only within a selected time window following a validated event. This ion gate allows the collection process to be synchronized with the prompt electron signal and provides the basis for suppressing pile-up from unrelated ionization events.

## 4 Principle of operation

### 4.1 Ion Chemistry and Charge Transfer

Primary ionization in xenon produces  $\text{Xe}^+$ , which rapidly converts to  $\text{Xe}_2^+$  through three-body association:



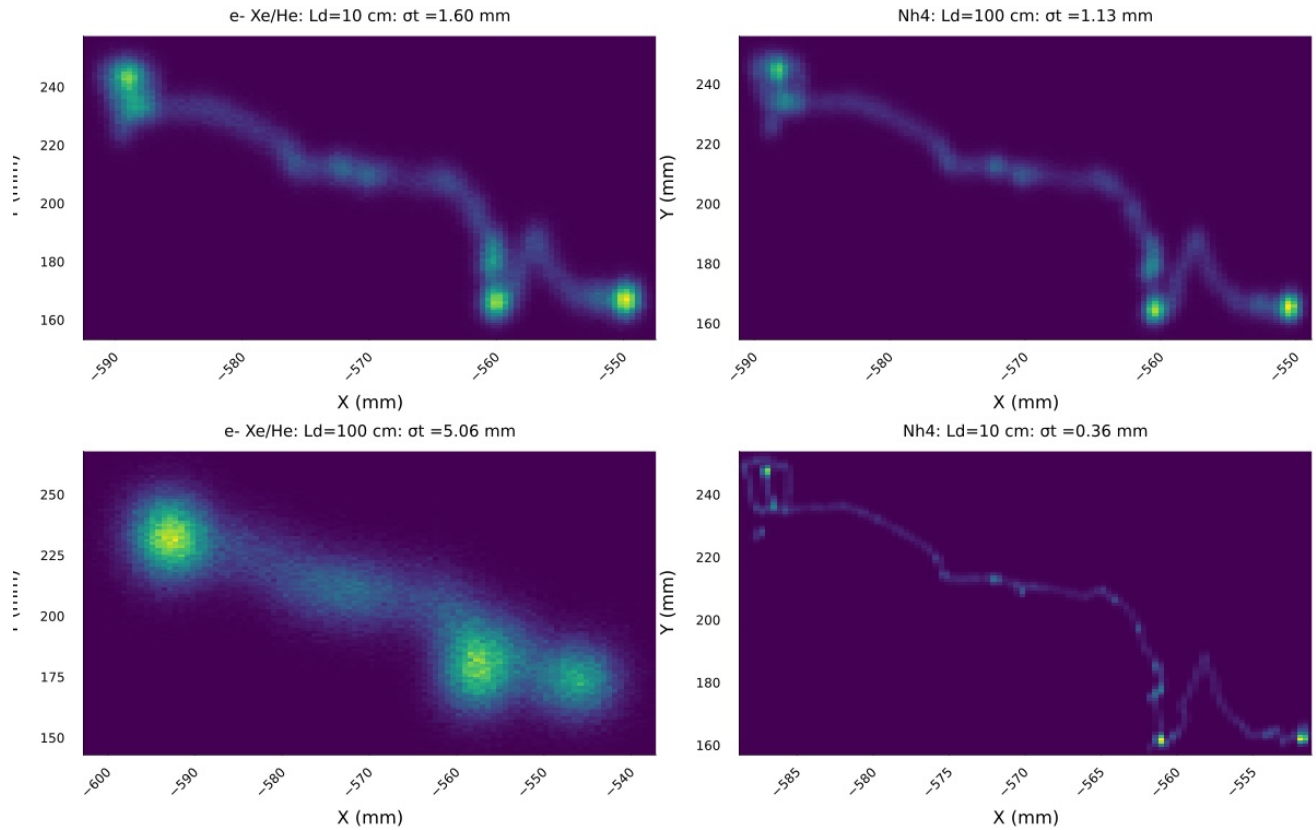
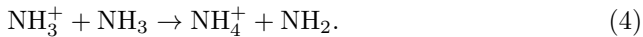
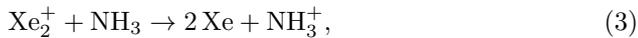


**Fig. 5** The diffusion in ion and electron tracks is anticorrelated. The upper panel shows the case in which the electrons are near the anode (10 cm), and thus ions are far away from the cathode (100 cm); the bottom panel shows the inverse case. Ions are close to the cathode (10 cm) and thus electrons are far from the anode (100 cm). The availability of the ion track allows a uniform topological reconstruction across the detector.

Trace amounts of ammonia convert the primary xenon ions into ammonium ( $\text{NH}_4^+$ ) through a rapid two-step mechanism: first, charge transfer from  $\text{Xe}_2^+$  to  $\text{NH}_3$  forming  $\text{NH}_3^+$ , followed by proton transfer with a second  $\text{NH}_3$  molecule to produce  $\text{NH}_4^+$



Laboratory data show that both processes are nearly collision-limited, with rate constants  $k_{ct} \approx 6 \times 10^{-10} \text{ cm}^3 \text{ molecule}^{-1} \text{ s}^{-1}$  for the  $\text{Xe}_2^+ + \text{NH}_3$  charge-transfer channel [37] and  $k_{pt} \approx 1.8 \times 10^{-9} \text{ cm}^3 \text{ molecule}^{-1} \text{ s}^{-1}$  for the proton transfer step [38]. Both reactions are exothermic by roughly 1–2 eV.

Let us consider an addition of a mole fraction  $f = 100$  ppb of  $\text{NH}_3$  to the xenon. At  $T \simeq 20$  °C and  $P = 30$  bar the xenon number density is  $n_{\text{Xe}} \approx 9 \times 10^{20} \text{ atoms/cm}^3$ , therefore  $n_{\text{NH}_3} = f \cdot n_{\text{Xe}} \approx 9 \times 10^{13} \text{ atoms/cm}^3$ . Thus, for the charge-transfer step

of eq. (3) we obtain:

$$\tau_{ct} = \frac{1}{k_{ct} \cdot n_{\text{NH}_3}} \approx \frac{1}{(6 \times 10^{-10})(9 \times 10^{13})} \simeq 18.5 \mu\text{s},$$

while for the proton-transfer step of eq. (4) we obtain a reaction time:

$$\tau_{pt} = \frac{1}{k_{pt} \cdot n_{\text{NH}_3}} \approx \frac{1}{(1.8 \times 10^{-9})(9 \times 10^{13})} \simeq 6 \mu\text{s},$$

Thus, both steps are completed in less than 100  $\mu\text{s}$  at  $5\tau$ , which is orders of magnitude shorter than ion drift times, ensuring near-complete conversion of the positive charge to  $\text{NH}_4^+$  before arrival at the cathode. Notice that full conversion will happen also very fast with much smaller amounts of  $\text{NH}_3$  (e.g., 10 ppb will convert the xenon ions in about 100  $\mu\text{s}$ , while conversion with 1 ppb only requires 1 ms, still three orders of magnitude smaller than drift time). It follows that one has considerable tolerance in the amount of ammonia added to the detector.

## 4.2 Transport Properties

The ion mobility  $\mu$  is defined as the proportionality constant between the drift velocity  $v_d$  and the electric field  $E$ :

$$v_d = \mu E. \quad (5)$$

In the low-field (thermal) regime,  $\mu$  depends on the ion–neutral collision frequency can be expressed [39] as

$$\mu = \frac{3q_e}{16N} \sqrt{\frac{2\pi}{m_r k_B T}} \frac{1}{\Omega(T)}, \quad (6)$$

where  $q_e = 1.602 \times 10^{-19}$  C,  $N$  is the gas number density, and  $m_r$  the ion–neutral reduced mass, and  $\Omega(T)$  the momentum-transfer collision integral. The neutral polarizability  $\alpha$  determines the strength of the long-range polarization potential  $V(r) = -\frac{1}{2}\alpha e^2 r^{-4}$ .

### Mobility in Argon at STP

From [40], the reduced mobility for  $\text{NH}_4^+$  in Ar is  $K_0 \approx 2.28 \pm 0.1 \text{ cm}^2 \text{ V}^{-1} \text{ s}^{-1}$  at STP. The corresponding mobility at 20 °C and 1 bar is:

$$\begin{aligned} \mu(20 \text{ °C}, 1 \text{ bar}) &= K_0 \frac{T}{T_0} \frac{P_0}{P} = (2.28 \pm 0.1) \times \frac{293}{273} \\ &\approx 2.5 \pm 0.11 \text{ cm}^2 \text{ V}^{-1} \text{ s}^{-1}. \end{aligned} \quad (7)$$

### Extrapolating from Argon to Xenon at the same (T, P)

For interactions dominated by polarization forces, the momentum-transfer integral scales as  $\Omega(T) \propto (\alpha/T)^{1/2}$ , yielding the approximate scaling:

$$\frac{\mu_B}{\mu_A} \simeq \sqrt{\frac{m_{r,A}}{m_{r,B}}} \sqrt{\frac{\alpha_A}{\alpha_B}}, \quad (8)$$

where  $m_r$  is the ion–neutral reduced mass and  $\alpha$  the neutral polarizability.

Using standard gas-phase polarizabilities [41]:

$$\alpha_{\text{Ar}} = 1.6411 \text{ \AA}^3, \quad \alpha_{\text{Xe}} = 4.044 \text{ \AA}^3, \quad (9)$$

gives  $\alpha_{\text{Ar}}/\alpha_{\text{Xe}} \approx 0.41$ . For  $\text{NH}_4^+$ ,  $m_i = 18$  u, while  $m_g^{\text{Ar}} = 40$  u and  $m_g^{\text{Xe}} = 131$  u, giving  $m_{r,\text{Ar}} \approx 12.4$  u and  $m_{r,\text{Xe}} \approx 15.8$  u, or  $m_{r,\text{Ar}}/m_{r,\text{Xe}} \approx 0.78$ . The mobility ratio is then  $\mu_{\text{Xe}}/\mu_{\text{Ar}} \approx 0.57$ .

At 20 °C and 1 bar:

$$\mu_{1\text{bar}}^{\text{Xe}} \approx 0.57 \times (2.50 \pm 0.11) \approx 1.42 \pm 0.06 \text{ cm}^2 \text{ V}^{-1} \text{ s}^{-1}. \quad (10)$$

### Pressure scaling

In the low- $E/N$  regime,  $\mu \propto 1/N \propto 1/P$  (for fixed  $T$ ), hence:

$$\mu_{30\text{bar}}^{\text{Xe}} \approx \frac{\mu_{1\text{bar}}^{\text{Xe}}}{30} \approx (0.047 \pm 0.001) \text{ cm}^2 \text{ V}^{-1} \text{ s}^{-1}. \quad (11)$$

### Drift velocity

For  $E = 400 \text{ V cm}^{-1}$ :

$$v_d = \mu E \approx 0.05 \times 400 \approx 20 \text{ cm s}^{-1}, \quad (12)$$

so drifting from the edge of the fiducial region (20 cm from the cathode) requires  $\approx 0.5$  s, while drifting the full length of the chamber would take 5 seconds.

### Diffusion

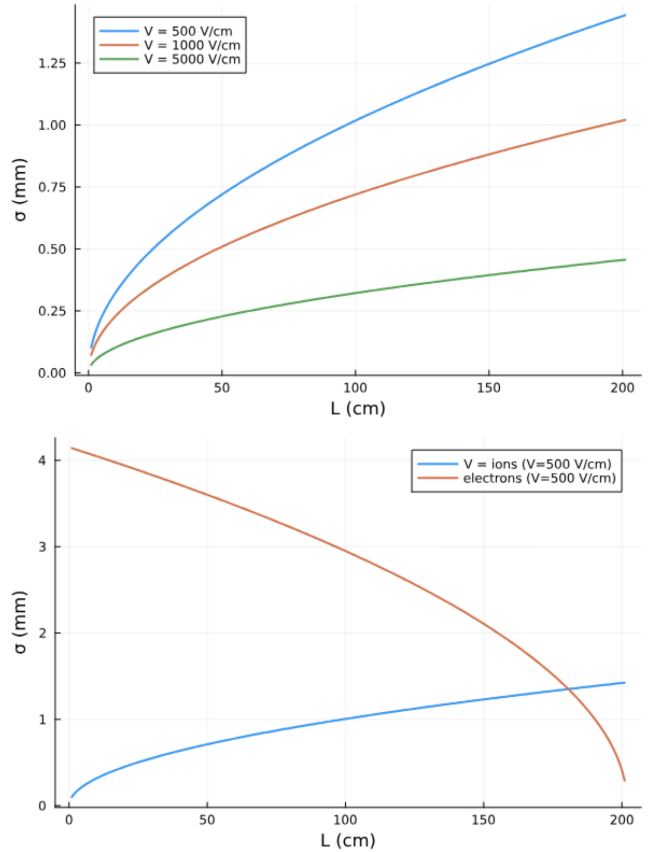


**Fig. 6** Top: diffusion of the ion track as a function of  $L$  for three different drift fields. Bottom: the diffusion of ions and electrons is anti-correlated ( $L$  is the distance to the node).

Assuming ions remain thermal,  $D = \mu k_B T / q_e$ ,

$$\sigma = \sqrt{2Dt} = \sqrt{\frac{2k_B T}{q_e} \frac{L}{E}}$$

Figure 6 (left) shows the diffusion of the ion track as a function of the drift length for three different drift fields. Notice that a drift field of 500 V/cm requires a potential difference between the anode and the gate of 100 kV, a high, but achievable value at large pressure, where the buffering of the noble gas is very large. A drift field of 1000 V/cm would be very challenging, while larger drift fields would require substantial technological developments.

Figure 6 (right) shows the anti-correlation between the electron and ion tracks, where  $L$  is the distance to the anode. Notice that for most of the drift length, the ion track has a much smaller diffusion than the electron track. However, near the anode, both tracks can be combined to further reduce the diffusion.

#### 4.3 VUV Absorption in Primary and Secondary Scintillation

The  $\text{Xe}_2^*$  excimer responsible for both primary (S1) and electroluminescent (S2) emission decays predominantly at 172 nm. Ammonia ( $\text{NH}_3$ ) absorbs strongly in this region, with cross sections  $\sigma_{\text{abs}} \sim 10^{-18} \text{ cm}^2$  [42] corresponding to dissociative excitation. Both S1 and S2 photons can, in principle, be absorbed by trace  $\text{NH}_3$  admixtures.

Primary scintillation photons are emitted throughout the TPC volume and may traverse meter-scale distances before reaching the photosensors. Electroluminescent photons emitted backward follow similar paths.

The attenuation length for VUV photons in Xe with a trace  $\text{NH}_3$  admixture is

$$\lambda_{\text{abs}} = \frac{1}{n_{\text{NH}_3} \sigma_{\text{abs}}} = \frac{1}{f n_{\text{Xe}} \sigma_{\text{abs}}}. \quad (13)$$

Plugging in  $f = 100 \text{ ppb}$ ,  $n_{\text{Xe}} \approx 9 \times 10^{20} \text{ atoms/cm}^{-3}$ , then  $n_{\text{NH}_3} \approx 9 \times 10^{13} \text{ molecules/cm}^{-3}$ . For a representative  $\text{NH}_3$  cross section at 172 nm  $\sigma_{\text{abs}} \approx 10^{-18} \text{ cm}^2$ :

$$\lambda_{\text{abs}} = \frac{1}{(9 \times 10^{13})(10^{-18})} \approx 1.1 \times 10^4 \text{ cm}. \quad (14)$$

For a 200 cm path,

$$\frac{I(L)}{I_0} = \exp\left(-\frac{L}{\lambda_{\text{abs}}}\right) = \exp\left(-\frac{200}{1.1 \times 10^4}\right) \sim 0.98, \quad (15)$$

resulting in a tiny loss of light at the maximum attenuation. For smaller concentrations (e.g, 10 ppb) the loss of light is totally negligible.

#### 4.4 Electron Attachment in Xe- $\text{NH}_3$ Mixtures

A possible concern when introducing molecular additives into xenon gas is electron attachment, which could shorten the electron lifetime and degrade the charge collection efficiency.

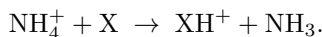
Electron attachment to  $\text{NH}_3$  proceeds mainly via *dissociative electron attachment* (DEA) resonances at electron energies of approximately 5.5 eV and 10.5 eV [43]:



At sub-eV energies, where electrons drift thermally in a TPC under moderate reduced fields ( $E/N \lesssim 5 \text{ Td}$ ), these channels are energetically closed and the attachment cross section is negligible. Therefore,  $\text{NH}_3$  behaves as a *non-electronegative* additive, in contrast with species such as  $\text{O}_2$ ,  $\text{H}_2\text{O}$ , or  $\text{SF}_6$ , which exhibit strong near-zero-eV resonances.

#### 4.5 Effects of Contaminants on $\text{NH}_4^+$

A priori  $\text{NH}_4^+$  can react in the gas phase with a neutral impurity  $X$  (such as  $\text{O}_2$ ,  $\text{CO}_2$ , or  $\text{H}_2\text{O}$ ) via proton transfer:



Whether this reaction can occur at thermal energies is determined by the sign of the Gibbs energy associated to this process, which can be easily estimated from tabulated gas-phase basicities (GB), see Table 2 [44].<sup>2</sup>

Accordingly, the Gibbs energy change for proton transfer from  $\text{NH}_4^+$  to a potential impurity is

$$\Delta G = \text{GB}(\text{NH}_3) - \text{GB}(X).$$

Hence

- If  $\text{GB}(X) > \text{GB}(\text{NH}_3)$ , then  $\Delta G < 0$  and proton transfer can proceed spontaneously.
- If  $\text{GB}(X) < \text{GB}(\text{NH}_3)$ , then  $\Delta G > 0$  and the reaction cannot occur thermally.

Looking at the values in Table 2, it is evident that all the potential impurities (e.g.,  $\text{H}_2\text{O}$ ,  $\text{CO}_2$ ,  $\text{O}_2$ ,  $\text{N}_2$ ,  $\text{CO}$ ,  $\text{H}_2$ ,  $\text{CH}_4$ ,  $\text{CH}_3\text{CN}$  or  $\text{CH}_3\text{OH}$ ) present a gas-phase basicity significantly smaller than that of  $\text{NH}_3$ ; thus proton transfer will be forbidden in the gas phase. Some

<sup>2</sup>We adopt the standard IUPAC gas-phase convention and define gas-phase basicity as the negative of the Gibbs energy change associated with the reaction  $X + \text{H}^+ \rightarrow \text{XH}^+$ .

of them (e.g.,  $\text{H}_2\text{O}$ ,  $\text{CH}_3\text{CN}$  or  $\text{CH}_3\text{OH}$ ) would interact with  $\text{NH}_4^+$ , but only through weak, reversible clustering. Species with  $\text{GB} > \text{GB}(\text{NH}_3)$ , such as certain amines, can potentially react with  $\text{NH}_4^+$  in gas phase. However, amines are very efficiently suppressed by hot getters, probably at the level of ppt concentrations. Electron-transfer neutralization of  $\text{NH}_4^+$  by impurities is energetically disfavored owing to the very low ionization potential of  $\text{NH}_4^+$  and is therefore expected to occur with a negligible probability under the conditions considered here.

Tetraphenyl butadiene (TPB,  $\text{C}_{28}\text{H}_{22}$ ) is a large aromatic hydrocarbon, extensively used as a wavelength shifter [45, 46]. It is a solid at room temperature, with extremely low vapor pressure ( $\ll 10^{-12}$  bar). Its gas-phase concentration in xenon is therefore negligible. Even if present in trace amounts, its gas-phase basicity is presumably comparable to that of other polycyclic aromatics and does not exceed  $\text{GB}(\text{NH}_3)$ . It follows that TPB should not affect the drift of  $\text{NH}_4^+$  in the gas phase.

**Table 2** Approximate gas-phase basicities of selected species (298 K). Data from ref. [44].

Species	GB [kJ/mol], 298 K
$(\text{CH}_3)_3\text{N}$	918.1
pyridine	898.1
$(\text{CH}_3)_2\text{NH}$	896.5
<b><math>\text{NH}_3</math></b>	<b>854.0</b>
$\text{CH}_3\text{CN}$	748.0
$\text{C}_6\text{H}_6$	725.4
$\text{CH}_3\text{OH}$	724.5
$\text{H}_2\text{O}$	660.0
$\text{CO}$	562.8
$\text{CH}_4$	520.0
$\text{CO}_2$	515.8
$\text{N}_2$	464.5
$\text{O}_2$	396.3
$\text{H}_2$	394.7

## 5 The ion track detector

The ion track detector is composed of four main components: the Molecular Ion Detector, the Magnetically-Activated Molecular Apparatus, the Transport and Shelving System, and the Ion Scanning Microscope.

**The Molecular Ion Detector (MID)** consists of:

1. A square carrier plate (CP),  $10 \times 10 \text{ cm}^2$ , large enough to amply contain an ion track (the typical track length at 30 bar is  $\sim 5 \text{ cm}$ , thus about 10

cm size). The CP moves along a rail by magnetic actuation.

2. A molecular target (MT), based on a VCC (Virtual Cathode Chamber) [47, 48] (figure 7). The VCC consists of a substrate made of resistive material, a conductive film in the back face of the substrate acting as a cathode, and anode strips in the front face. Electrostatic focusing is used to guide the incoming ions onto the active strip regions of the detector, increasing the local ion density at the sensor surface and thereby improving both capture efficiency and signal-to-noise while minimizing the required read-out area. The strips are 10 cm long and  $50 \mu\text{m}$  wide and are spaced at a pitch of  $250 \mu\text{m}$ . The molecular sensors are deposited on top of the anode strips. The MT can be inserted (removed) in a holder fixed to the CP.

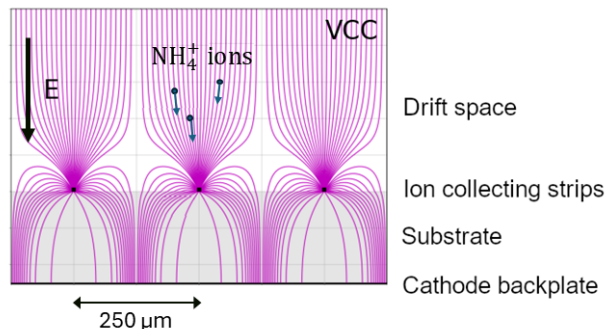


**Fig. 7** In the MID, ions are focused onto the strips of a VCC microstructure similar to that shown in the figure.

**The Magnetically Activated Molecular Apparatus (MAMA)** is shown in figure 8. The simplest realization of the device is a guide that moves left to right on magnetically activated rails, and an MID that moves up to down, also by magnetic activation, on the guide. In practice, the device will contain two or more guides, and each guide will contain two MIDs, to reduce the distance traveled by the MID to intercept the ion.

**The Transport and Shelving System (TSS)** has the following roles:

1. It can place and/or remove the MT in the MID. Each time a trigger activates and data is collected, the MT is removed from the MID (after the device returns to its parking position), and a new MT is placed in the MID.
2. It takes the MT to the microscope system for scanning, after a trigger.
3. It stores the MT in a shelf after scanning.

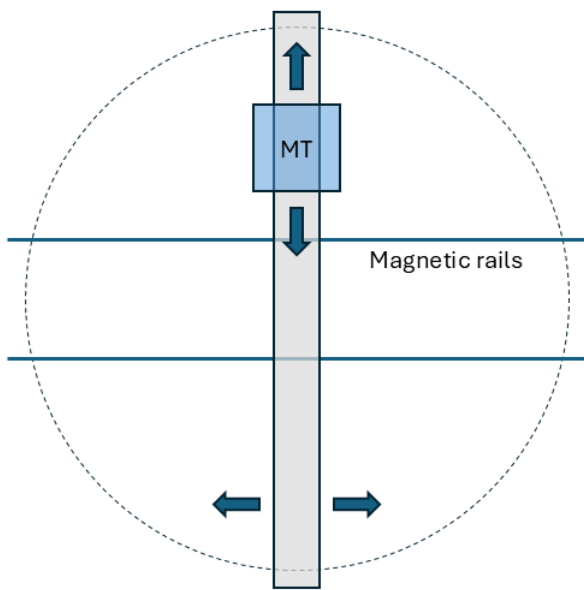


**Fig. 8** A sketch of the Magnetically Activated Molecular Apparatus (MAMA).

**The Ion Scanning Microscope (ISM)** consists of a microscope coupled via optical fibers to an excitation laser. The microscope includes a pressure-resistant objective connected to a CCD camera, similar to those developed in the context of the Barium Tagging R&D Program [49] and the necessary instrumentation to perform a fast scanning of the molecular target.

Consider now a  $\beta\beta 0\nu$  decay occurring at coordinates  $(x, y, z)$  in the ITACA detector. For illustration, take  $z = 100$  cm (e.g. in the middle of the TPC). The electron track is collected by the SiPMs instrumenting the anode approximately 1 ms after  $t_0$ . Afterwards, one has 2.5 seconds to measure the event energy and perform a rough reconstruction of the topology (0.5 seconds if the event occurs at the edge of the fiducial volume,  $L = 190$  cm).

An event is classified as a  $\beta\beta 0\nu$  candidate if:

1. The event energy lies in the ROI (e.g.  $\pm 25$  keV around  $Q_{\beta\beta}$ ).
2. A single track (with no disconnected energy depositions) is reconstructed.

If both conditions are fulfilled, then:

1. The event barycenter is computed in the anode plane,  $P = (x_b, y_b, z_a)$ .
2. The barycenter is projected to the detection region, located near the cathode at  $z = z_c$ , yielding  $P' = (x_b, y_b, z_c)$ .
3. The MAMA system positions the MID in  $P'$ , captures the ion track and then is retracted to its parking position.

4. The TSS takes the MT from its holder in the MID and introduces a new MT. Then transports the MT to the ISM where is scanned. After scanning the MT is placed in a storage shelf.
5. The ISM scans the MT and reconstructs the track.

### 5.1 Molecular sensors

The same techniques under development for  $\text{Ba}^{2+}$  tagging could be applied here for  $\text{NH}_4^+$  sensing, e.g. the use of a fluorescent chemical sensor offering a clear luminescent response to the ions.

Concerning the type of sensors to be employed, fortunately, the development of luminescent sensors for quaternary ammonium cations is a mature area of research. Its development is driven by the ubiquity of these ions in many biologically active molecules and by their participation in several biological processes ( $\text{NH}_4^+$  is a common cellular metabolite and key for the correct cellular pH balance) [50]. An overview of the different families of sensors already developed for these ions reveals crown-ethers, aza-crown ethers and related cryptands [51] among the most recurrent binding motives [50]. Actually, the affinity of these macrocyclic receptors for quaternary ammonium cations is well established since the first reports on crown ethers and the early developments of host-guest chemistry [52–54]. In these examples, the recognition of ammonium ions relies on the presence of hydrogen bonds between the strongly polarized N-H bonds and the lone pairs of the N or O atoms in the receptor, helped by the appropriate steric complementarity (dictated by the size and flexibility of the macrocyclic receptor), being 18-crown-6 type the optimal size and shape for binding  $\text{NH}_4^+$  or primary ammonium ions [51, 55].

Notably, 1-aza-18-crown-6 ethers (and related compounds) are one of the sensors extensively studied within the NEXT Barium Tagging R&D Program. Therefore, all the know-how already developed can be directly transferred to this new configuration (and vice versa). Having established azacrown ethers as binding units, one can construct off/on, bicolor or time-resolved luminescence sensors depending on the nature of the fluorophore employed. Considering a turning-on response as the most simple sensing mechanism, a naphthalimide derivative (NAPH3, see Figure 9), formerly studied for  $\text{Ba}^{2+}$  tagging, can be used as a representative example. In this sensor, in the off state (no ion present) the luminescence is quenched due to a Photoinduced Electron Transfer mechanism (PET) from the azacrown ether to the naphthalimide moiety. This process is deactivated upon ion binding.

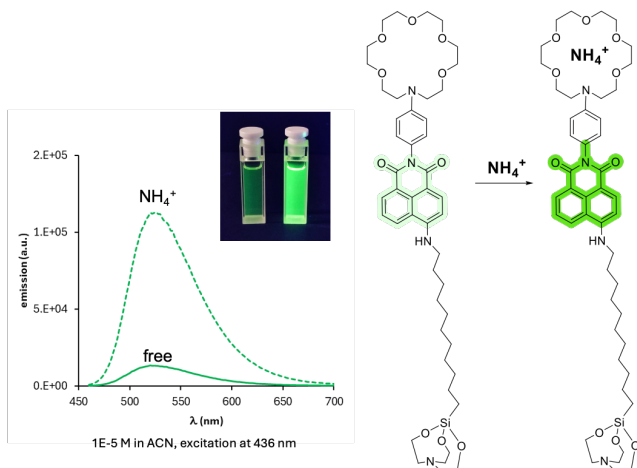


**Fig. 9** Emission spectra of the free and chelated species (with  $\text{NH}_4^+$ ) of NAPH3 (Naphthalimide) sensors.

Figure 10 shows a prototype of a molecular target, containing a layer of NAPH3 sensors functionalized in a coverslip. The response to laser interrogation of the MT is shown before chelating the molecular sensors with  $\text{NH}_4^+$  (left panel) and after (right panel), showing a strong enhancement of the light emission and illustrating the soundness of the concept.

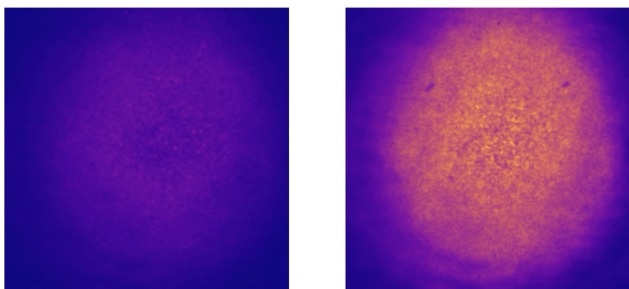


**Fig. 10** Left panel: response to laser interrogation of a molecular target containing a layer of NAPH3 sensors functionalized in a coverslip. Light emission is very weak, since the PET mechanism quenches fluorescence. Right panel: response to laser interrogation after chelating the molecular target with  $\text{NH}_4^+$  ions, showing a strong enhancement of light emission.

## 5.2 Measuring the ion track

The ion track is scanned with a microscope coupled to a suitable excitation laser, a pressure-resistant objective of high NA (0.95) and a high-resolution camera.

Figure 11 illustrates how a track segment is scanned in the VCC. The first step is to project the electron track envelope into the VCC. Then the microscope moves along the strips, recording frames of  $50 \times 250 \mu\text{m}^2$ . Consider a typical track in the VCC. The

track length is about 50 mm and its width about 4 mm (for a  $\sigma_t = 1 \text{ mm}$ ). Suppose that the track is parallel to the strips. Then, its envelope contains about 16 strips, and scanning each strip requires 200 frames, resulting in a total of 3200 frames. If the track is perpendicular to the strips, the number of strips is the same.

The molecular sensor layers (MSL) are deposited on each strip. The MSL is characterized by two parameters. Its surface density ( $\rho_s$ ), and the fraction of free molecules that respond to the laser excitation ( $f_b$ ). Both parameters are being investigated in the context of the Barium-tagging R&D. For a fully packed monolayer  $\rho_s \sim 10^6 \text{ molecules}/\mu\text{m}^2$ , but such a dense arrangement may result in collective effects, and a density of  $\rho_s \sim 10^5 \text{ molecules}/\mu\text{m}^2$  (molecules spaced about 3 nm) appears to be a much better option. Depending on the structure of MSL (which can be designed co-functionalizing sensors with passive components), densities of  $\rho_s \sim 10^4 \text{ molecules}/\mu\text{m}^2$  may be feasible, hopefully keeping high ion trapping efficiency.

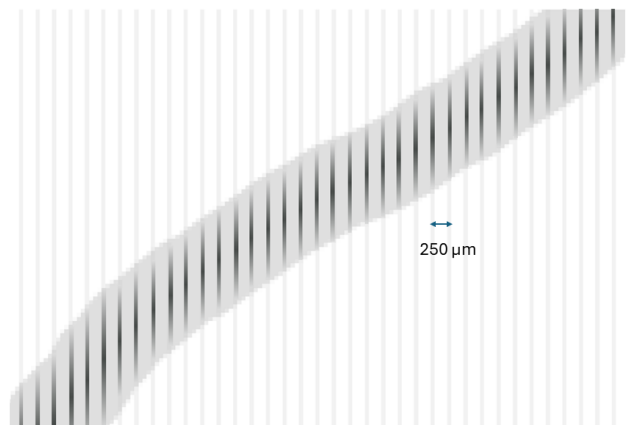


**Fig. 11** A segment of the track being sampled by the strips in the VCC.

Reducing as much as possible the fraction of molecules that respond to excitation light when not chelated with the incoming ion,  $f_b$ , is also an active area of research. PET sensors, on the other hand can yield background fractions below  $f_b \sim 10^{-3}$  [56].

For illustration purposes, we have run a simulation with the following parameters.

- Example sensor: NAPH3 (Naphthalimide).
- MID as described above: frames of  $50 \times 250 \mu\text{m}^2$ .
- Scanning time per frame: 0.1 s.
- Laser power: 10 mW.
- $\rho_s \times f_b \sim 10^2 \text{ molecules}/\mu\text{m}^2$  (for instance,  $\rho_s \sim 10^5 \text{ molecules}/\mu\text{m}^2$  and  $f_b \sim 10^{-3}$ ).

Figure 12 shows the number of photons per active molecule emitted during the exposition time (0.1 sec-

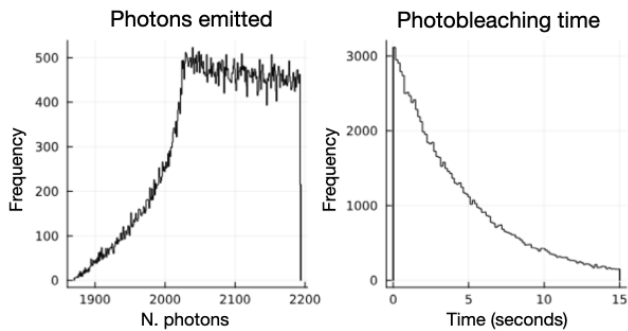


**Fig. 12** Left: Number of photons per active molecule emitted during the exposition time (0.1 second) in each pin; right: photobleaching time.

ond), which is chosen to be small compared with photobleaching time. The asymmetry in the distribution of the number of emitted photons is related with the non-uniformity of the beam (simulated as a gaussian beam) illumination of the strip.

Figure 13 shows one example of our simulations. The upper row: shows the electron and ions tracks corresponding to a  $\beta\beta 0\nu$  event after diffusion of 50 cm. The bottom row shows the reconstruction of the ion track. In the bottom left panel we record only the light produced by the chelated molecules (thus, the fraction of active background molecules is forced to zero). In the bottom right panel we show the image obtained recording the photons emitted by the chelated molecules as well as the fraction of active molecules in the layer. Notice that, although the background noise is visible, the main features of the track, and in particular the clean structure of the blobs, remain unchanged.

It appears, therefore, possible to measure the ion track with high signal to noise. The time associated to the measurement is of the order of 300 s, which is perfectly affordable since the scanning of the ion track only occurs for  $\beta\beta 0\nu$  candidates.

Given the slow drift velocity of the ions, gas motion associated with continuous purification, thermal gradients, or mechanical actuation could, in principle, affect the ion signal in two ways: by introducing uncertainties in the ion arrival time at the detector and by distorting the reconstructed ion topology. In the ITACA concept, the timing aspect is mitigated by event-driven gating, whereby the ion-collection window is opened only for events that pass the energy selection and the prompt electron-track topology criteria, thereby strongly suppressing pile-up from unrelated ions. Concerning topology, gas recirculation in large high-pressure xenon TPCs is typically operated at low flow rates designed to ensure smooth, quasi-laminar conditions [12]. Under such conditions, gas motion is expected to induce primarily coherent displacements or

mild distortions of the ion track rather than topology scrambling, manifesting as a modest degradation of spatial resolution rather than a loss of topological discrimination.

## 6 Enhancement of the sensitivity

The measurement of the ion track will enhance the overall sensitivity of the GXeEL technology along two complementary lines. On one hand, the reduced diffusion permits a better discrimination between near-by floating energy depositions (for example the characteristic 30 keV X-ray emitted in  $^{214}\text{Bi}$  decays) and the main track, and on the other, it improves the discrimination between “single electrons” and “double electrons”, since the two blobs are easier to recognize. This enhanced topological separation is particularly relevant for suppressing backgrounds that intrinsically produce single-electron recoils, including those arising from elastic scattering of solar neutrinos, which constitute a background for next-generation ton-scale xenon detectors [57]. In addition, topology plays a crucial role in mitigating backgrounds from charged-current solar neutrino interactions on  $^{136}\text{Xe}$ , which produce  $^{136}\text{Cs}$  followed by  $\beta$  decays with endpoint energies near the ROI [58].

To quantify the improvement in sensitivity relative to that of a GXeEL TPC operating with pure Xe and a Xe/He gas mixture, signal ( $0\nu\beta\beta$ ) and background (individual gamma rays of energy 2.447 MeV) events were simulated uniformly in the active region of the detector. The resulting energy depositions were recorded on a 3D grid of “voxels” for input to a Sparse Convolutional neural network [59]. The network was trained to classify the events into signal and background using approximately 88,500 of each event type in the training set, 50,000 in the validation set, and 20,000 in the test set. This process was repeated for voxel sizes of  $1 \times 1 \times 1 \text{ mm}^3$ ,  $3.5 \times 3.5 \times 3.5 \text{ mm}^3$ , and  $10 \times 10 \times 10 \text{ mm}^3$  to model the diffusion and reconstruction accuracy in the case of  $\text{NH}_3$ , a GXeEL TPC filled with a Xe/He mixture, and with pure Xe, respectively.

Figure 14 shows the ROC curves obtained in this study. Using only the electron track yields an area under the curve (AUC) of 0.96 in pure xenon. Including the ion track information improves the AUC to 0.992, corresponding to a factor-of-5 gain in sensitivity, defined as the ratio of  $1 - \text{AUC}$  between the two cases. A further improvement arises from the enhanced separation between floating gamma interactions and the main track. In particular, we find an additional factor-of-4 background rejection for  $^{214}\text{Bi}$  gamma rays —the most

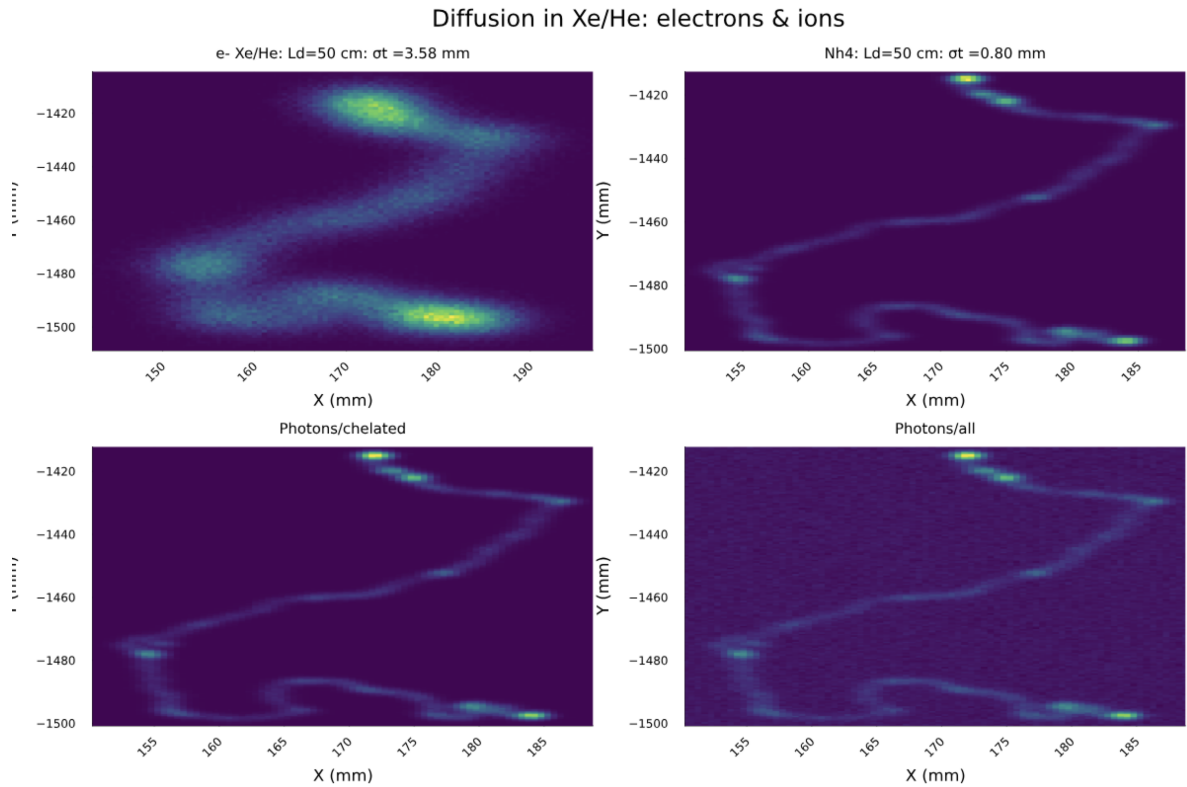


**Fig. 13** Upper row: electron and ions tracks corresponding to a  $\beta\beta 0\nu$  event after diffusion of 50 cm; bottom row: reconstruction of the ion track. The bottom left panel shows the image obtained recording the photons emitted only by the chelated molecule. The bottom right panel shows the image obtained recording the photons emitted by the chelated molecules as well as the fraction of active molecules in the layer.

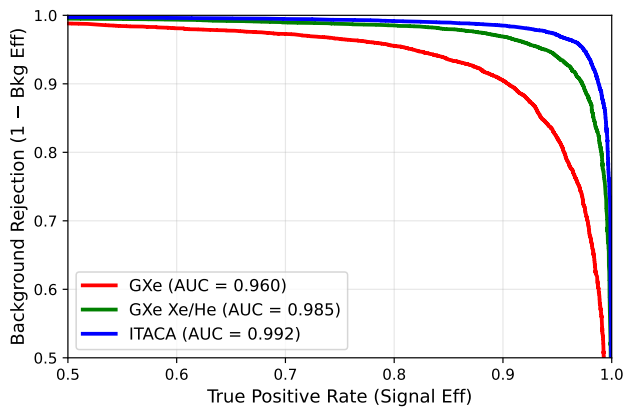


**Fig. 14** ROC curves for the ITACA detector (blue) and a GXe detector operating with pure Xe (red) and a Xe/He mixture (green).

dangerous background due to their proximity to  $Q_{\beta\beta}$ —leading to an overall  $\times 20$  improvement.

## 7 Conclusions

Measurement of ion tracks with a diffusion of order 1 mm appears feasible in a GXeEL detector. Imple-

menting this concept requires extending the current technology to include controlled trace concentrations of  $\text{NH}_3$  and an ion-detection system located in the cathode region.

In addition, the proposed technique is potentially compatible with barium tagging. Since  $\text{Ba}^{2+}$  ions are expected to drift at a velocity different from that of  $\text{NH}_4^+$  [60], a sequential collection scheme is in principle possible in which the  $\text{NH}_4^+$  ion track is first recorded on the molecular target and, subsequently, the same target is translated by a small distance such that the delayed  $\text{Ba}^{2+}$  ion is intercepted on an unoccupied region of the sensor surface. Such a sequential scheme could enable the combination of ion-track topology with barium tagging, thereby providing an additional handle for background rejection, even in scenarios where the barium-tagging efficiency is limited.

The additional discrimination provided by the sharply defined ion track further has the potential to reduce the backgrounds by an additional order of magnitude compared with the standard GXeEL technology. This enhanced rejection capability is crucial to achieving the ultra-low background levels required to probe the normal neutrino-mass hierarchy.

**Acknowledgements** The authors would like to acknowledge support from the following agencies and institutions: the European Research Council (ERC) under Grant Agreement No. 951281-BOLD, the MCIN/AEI of Spain and ERDF A way of making Europe under grant PID2024-161553NB-C51, the Dpt. of Science, Universities and Innovation of the Basque Government through the 2025 grant to the DIPC Neutrino Physics Laboratory. The experimental part of this work was supported by project PID2022-139760NB-I00 funded by MCIN/AEI/10.13039/501100011033 and FEDER A way of making Europe. JR acknowledges support from the Generalitat Valenciana of Spain under grant CIDEXG/2023/16. ME acknowledges support from the Basque Government under grant PRE\_2025\_2\_0146. Discussions with our colleagues in the NEXT collaboration and the BOLD R&D program are warmly acknowledged.

## References

1. F. T. Avignone III, S. R. Elliott, and J. Engel. Double beta decay, Majorana neutrinos, and neutrino mass. *Rev. Mod. Phys.*, 80:481, 2008. [arXiv:0708.1033](#), [doi:10.1103/RevModPhys.80.481](#).
2. Michelle J. Dolinski, Alan W.P. Poon, and Werner Rodejohann. Neutrinoless Double-Beta Decay: Status and Prospects. *Ann. Rev. Nucl. Part. Sci.*, 69(Volume 69, 2019):219–251, 2019. URL: <https://www.annualreviews.org/content/journals/10.1146/annurev-nucl-101918-023407>, [arXiv:1902.04097](#), [doi:10.1146/annurev-nucl-101918-023407](#).
3. Juan José Gómez-Cadenas, Justo Martín-Albo, Javier Menéndez, Mauro Mezzetto, Francesc Monrabal, and Michel Sorel. The search for neutrinoless double-beta decay. *Riv. Nuovo Cim.*, 46(10):619–692, 2023. [doi:10.1007/s40766-023-00049-2](#).
4. S. Abe et al. Search for Majorana Neutrinos with the Complete KamLAND-Zen Dataset. 2024. [arXiv:2406.11438](#), [doi:10.48550/arXiv.2406.11438](#).
5. H. Acharya et al. First Results on the Search for Lepton Number Violating Neutrinoless Double Beta Decay with the LEGEND-200 Experiment. 2025. [arXiv:2505.10440](#).
6. V. Álvarez et al. The NEXT-100 experiment for neutrinoless double beta decay searches (Conceptual Design Report). 2011. [arXiv:1106.3630](#).
7. V. Álvarez et al. NEXT-100 Technical Design Report (TDR): Executive Summary. *JINST*, 7:T06001, 2012. [arXiv:1202.0721](#), [doi:10.1088/1748-0221/7/06/T06001](#).
8. V. Álvarez et al. Near-Intrinsic Energy Resolution for 30 to 662 keV Gamma Rays in a High Pressure Xenon Electroluminescent TPC. *Nucl. Instrum. Meth.*, A708:101–114, 2012. [arXiv:1211.4474](#), [doi:10.1016/j.nima.2012.12.123](#).
9. V. Álvarez et al. Radiopurity control in the NEXT-100 double beta decay experiment: procedures and initial measurements. *JINST*, 8:T01002, 2012. [arXiv:1211.3961](#), [doi:10.1088/1748-0221/8/01/T01002](#).
10. V. Álvarez et al. Ionization and scintillation response of high-pressure xenon gas to alpha particles. *JINST*, 1305:P05025, 2013. [arXiv:1211.4508](#), [doi:10.1088/1748-0221/8/05/P05025](#).
11. V. Álvarez et al. Initial results of NEXT-DEMO, a large-scale prototype of the NEXT-100 experiment. *JINST*, 8:P04002, 2013. [arXiv:1211.4838](#), [doi:10.1088/1748-0221/8/04/P04002](#).
12. C. Adams et al. The NEXT-100 Detector. 5 2025. [arXiv:2505.17848](#).
13. M. Pérez Maneiro et al. Demonstration of Sub-Percent Energy Resolution in the NEXT-100 Detector. 2025. [arXiv:2511.02467](#).
14. Shinichi Akiyama et al. In-situ high voltage generation with Cockcroft-Walton multiplier for xenon gas time projection chamber. 1 2025. [arXiv:2501.08554](#).
15. P. Ferrario et al. First proof of topological signature in the high pressure xenon gas TPC with electroluminescence amplification for the NEXT experiment. *JHEP*, 01:104, 2016. [arXiv:1507.05902](#), [doi:10.1007/JHEP01\(2016\)104](#).
16. R. Felkai et al. Helium–Xenon mixtures to improve the topological signature in high pressure gas xenon TPCs. *Nucl. Instrum. Meth.*, A905:82–90, 2018. [arXiv:1710.05600](#), [doi:10.1016/j.nima.2018.07.013](#).
17. A. F. M. Fernandes et al. Low-diffusion Xe-He gas mixtures for rare-event detection: Electroluminescence Yield. *JHEP*, 04:034, 2020. [arXiv:1906.03984](#), [doi:10.1007/JHEP04\(2020\)034](#).
18. A.D. McDonald et al. Electron drift and longitudinal diffusion in high pressure xenon-helium gas mixtures. *JINST*, 14(08):P08009, 2019. [arXiv:1902.05544](#), [doi:10.1088/1748-0221/14/08/P08009](#).
19. C. A. O. Henriques et al. Electroluminescence TPCs at the Thermal Diffusion Limit. *JHEP*, 01:027, 2019. [arXiv:1806.05891](#), [doi:10.1007/JHEP01\(2019\)027](#).
20. C. A. O. Henriques et al. Secondary scintillation yield of xenon with sub-percent levels of CO<sub>2</sub> additive for rare-event detection. *Phys. Lett.*, B773:663–671, 2017. [arXiv:1704.01623](#), [doi:10.1016/j.physletb.2017.09.017](#).
21. B. J. P. Jones, A. D. McDonald, and D. R. Nygren. Single Molecule Fluorescence Imaging as

- a Technique for Barium Tagging in Neutrinoless Double Beta Decay. *JINST*, 11(12):P12011, 2016. [arXiv:1609.04019](https://arxiv.org/abs/1609.04019), [doi:10.1088/1748-0221/11/12/P12011](https://doi.org/10.1088/1748-0221/11/12/P12011).
22. A. D. McDonald et al. Demonstration of Single Barium Ion Sensitivity for Neutrinoless Double Beta Decay using Single Molecule Fluorescence Imaging. *Phys. Rev. Lett.*, 120(13):132504, 2018. [arXiv:1711.04782](https://arxiv.org/abs/1711.04782), [doi:10.1103/PhysRevLett.120.132504](https://doi.org/10.1103/PhysRevLett.120.132504).
  23. P. Thapa, I. Arnquist, N. Byrnes, A. A. Denisenko, F. W. Foss, B. J. P. Jones, A. D. McDonald, D. R. Nygren, and K. Woodruff. Barium Chemosensors with Dry-Phase Fluorescence for Neutrinoless Double Beta Decay. 2019. [arXiv:1904.05901](https://arxiv.org/abs/1904.05901).
  24. Iván Rivilla, Borja Aparicio, Juan M. Bueno, David Casanova, Claire Tonnelé, Zoraida Freixa, Pablo Herrero, Celia Rogero, José I. Miranda, Rosa M. Martínez-Ojeda, Francesc Monrabal, Beñat Olave, Thomas Schafer, Pablo Artal, David Nygren, Fernando P. Cossío, and Juan J. Gómez-Cadenas. Fluorescent bicolour sensor for low-background neutrinoless double  $\beta$  decay experiments. *Nature*, 583(7814):48–54, July 2020. Number: 7814 Publisher: Nature Publishing Group. URL: <https://www.nature.com/articles/s41586-020-2431-5>, [doi:10.1038/s41586-020-2431-5](https://doi.org/10.1038/s41586-020-2431-5).
  25. Ane I. Aranburu, Mikel Elorza, Pablo R.G. Valle, Ariadna Pazos, Alexey Brodolin, Pablo Herrero-Gómez, J. Eduardo Barcelon, Gabriel Molina-Terriza, Francesc Monrabal, Celia Rogero, Fernando P. Cossío, Juan José Gómez-Cadenas, Claire Tonnelé, and Zoraida Freixa. Iridium-Based Time-Resolved Luminescent Sensor for Ba<sup>2+</sup> Detection. *ACS Sensors*, 10(4):2487–2498, 2025. PMID: 40213995. [arXiv:https://doi.org/10.1021/acssensors.4c01892](https://arxiv.org/abs/https://doi.org/10.1021/acssensors.4c01892), [doi:10.1021/acssensors.4c01892](https://doi.org/10.1021/acssensors.4c01892).
  26. Fernando Auria-Luna et al. Supramolecular chemistry in solution and solid–gas interfaces: synthesis and photophysical properties of monocolour and bicolour fluorescent sensors for barium tagging in neutrinoless double beta decay. *RSC Appl. Interfaces*, 2(1):185–199, 2025. URL: <http://dx.doi.org/10.1039/D4LF00227J>, [doi:10.1039/D4LF00227J](https://doi.org/10.1039/D4LF00227J).
  27. Zoraida Freixa, Iván Rivilla, Francesc Monrabal, Juan J. Gómez-Cadenas, and Fernando P. Cossío. Bicolour fluorescent molecular sensors for cations: design and experimental validation. *Phys. Chem. Chem. Phys.*, 23(29):15440–15457, 2021. URL: <http://dx.doi.org/10.1039/D1CP01203G>, [doi:10.1039/D1CP01203G](https://doi.org/10.1039/D1CP01203G).
  28. Pawan Thapa, Nicholas K. Byrnes, Alena A. Denisenko, James X. Mao, Austin D. McDonald, Charleston A. Newhouse, Thanh T. Vuong, Katherine Woodruff, Kwangho Nam, David R. Nygren, Benjamin J. P. Jones, and Jr. Foss, Frank W. Demonstration of selective single-barium ion detection with dry diazacrown ether naphthalimide turn-on chemosensors. *ACS Sens.*, 6(1):192–202, 2021. [doi:10.1021/acssensors.0c02104](https://doi.org/10.1021/acssensors.0c02104).
  29. P. Herrero-Gómez et al. Ba<sup>2+</sup> ion trapping using organic submonolayer for ultra-low background neutrinoless double beta detector. *Nature Commun.*, 13(1):7741, 2022. [arXiv:2201.09099](https://arxiv.org/abs/2201.09099), [doi:10.1038/s41467-022-35153-0](https://doi.org/10.1038/s41467-022-35153-0).
  30. C. J. Martoff, D. P. Snowden-Ifft, T. Ohnuki, N. Spooner, and M. Lehner. Suppressing drift chamber diffusion without magnetic field. *Nucl. Instrum. Meth. A*, 440:355–359, 2000. [doi:10.1016/S0168-9002\(99\)00955-9](https://doi.org/10.1016/S0168-9002(99)00955-9).
  31. D. P. Snowden-Ifft, C. J. Martoff, and J. M. Burwell. Low pressure negative ion drift chamber for dark matter search. *Phys. Rev. D*, 61:101301, 2000. [arXiv:astro-ph/9904064](https://arxiv.org/abs/astro-ph/9904064), [doi:10.1103/PhysRevD.61.101301](https://doi.org/10.1103/PhysRevD.61.101301).
  32. B. J. P. Jones, F. W. Foss, J. A. Asaadi, E. D. Church, J. deLeon, E. Gramellini, O. H. Seidel, and T. T. Vuong. The Ion Fluorescence Chamber (IFC): A new concept for directional dark matter and topologically imaging neutrinoless double beta decay searches. 2022. [arXiv:2203.10198](https://arxiv.org/abs/2203.10198).
  33. A. Simón et al. Application and performance of an ML-EM algorithm in NEXT. *JINST*, 12(08):P08009, 2017. [arXiv:1705.10270](https://arxiv.org/abs/1705.10270), [doi:10.1088/1748-0221/12/08/P08009](https://doi.org/10.1088/1748-0221/12/08/P08009).
  34. A. Simón et al. Electron drift properties in high pressure gaseous xenon. *JINST*, 13:P07013, 2018. [arXiv:1804.01680](https://arxiv.org/abs/1804.01680).
  35. C. Adams et al. Sensitivity of a tonne-scale NEXT detector for neutrinoless double beta decay searches. *JHEP*, 2021(08):164, 2021. [arXiv:2005.06467](https://arxiv.org/abs/2005.06467), [doi:10.1007/JHEP08\(2021\)164](https://doi.org/10.1007/JHEP08(2021)164).
  36. S. R. Soleti. Towards a fiber barrel detector for next-generation high-pressure gaseous xenon TPCs. *JINST*, 19(04):C04042, 2024. [arXiv:2312.05567](https://arxiv.org/abs/2312.05567), [doi:10.1088/1748-0221/19/04/C04042](https://doi.org/10.1088/1748-0221/19/04/C04042).
  37. D. J. Levandier and Y. K. Chiu. A guided ion beam study of the reactions of Xe<sup>+</sup> and Xe<sub>2</sub><sup>+</sup> with NH<sub>3</sub>. *Journal of Chemical Physics*, 133:154304, 2010. [doi:10.1063/1.3496668](https://doi.org/10.1063/1.3496668).
  38. Wayne E. Conaway, Takayuki Ebata, and Richard N. Zare. Vibrationally state-selected reactions of ammonia ions. III. NH<sub>3</sub><sup>+</sup> + NH<sub>3</sub> → NH<sub>4</sub><sup>+</sup> + NH<sub>2</sub>. *Journal of Chemical Physics*,

- 87(6):3453–3460, 1987. doi:10.1063/1.453084.
39. E. A. Mason and E. W. McDaniel. *Transport Properties of Ions in Gases*. John Wiley & Sons, New York, 1988.
40. Azra Abedi, Laleh Sattar, Mahtab Gharibi, and Larry A. Viehland. Investigation of temperature, electric field and drift-gas composition effects on the mobility of  $\text{nh}_4^+$  ions in he, ar,  $\text{n}_2$ , and  $\text{co}_2$ . *International Journal of Mass Spectrometry*, 370:101–106, 2014. URL: <https://www.sciencedirect.com/science/article/pii/S1387380614002206>, doi:10.1016/j.ijms.2014.06.014.
41. EA Mason and EW McDaniel. Tables of properties useful in the estimation of ion-neutral interaction energies. *Transport Properties of Ions in Gases, Chapter Appendix III*, pages 531–540, 1988.
42. F. Z. Chen, D. L. Judge, C. Y. Robert Wu, and John Caldwell. Low and room temperature photoabsorption cross sections of  $\text{NH}_3$  in the UV region. *Planetary and Space Science*, 47:261–266, 1999. doi:10.1016/S0032-0633(98)00074-9.
43. Thomas N. Rescigno, Carlos S. Trevisan, Ann E. Orel, Daniel S. Slaughter, Hiroshi Adaniya, Ali Belkacem, Marvin Weyland, Alexander Dorn, and C. W. McCurdy. Dynamics of dissociative electron attachment to ammonia. *Phys. Rev. A*, 93(5):052704, 2016. URL: <https://link.aps.org/doi/10.1103/PhysRevA.93.052704>, doi:10.1103/PhysRevA.93.052704.
44. Edward P. L. Hunter and Sharon G. Lias. Evaluated gas phase basicities and proton affinities of molecules: An update. *Journal of Physical and Chemical Reference Data*, 27(3):413–656, 1998. doi:10.1063/1.556018.
45. V. M. Gehman, S. R. Seibert, K. Rielage, A. Hime, Y. Sun, D. M. Mei, J. Maassen, and D. Moore. Fluorescence Efficiency and Visible Re-emission Spectrum of Tetraphenyl Butadiene Films at Extreme Ultraviolet Wavelengths. *Nucl. Instrum. Meth.*, A654:116–121, 2011. arXiv:1104.3259, doi:10.1016/j.nima.2011.06.088.
46. J. Haefner et al. Reflectance and fluorescence characteristics of PTFE coated with TPB at visible, UV, and VUV as a function of thickness. *JINST*, 18(03):P03016, 2023. arXiv:2211.05024, doi:10.1088/1748-0221/18/03/P03016.
47. M. Capeáns, W. Dominik, M. Hoch, L. Ropelewski, F. Sauli, L. Shekhtman, and A. Sharma. The virtual cathode chamber. *Nuclear Instruments and Methods in Physics Research Section A*, 400:17–23, 1997.
48. A. Breskin. Novel electron and photon recording concepts in noble-liquid detectors. *Journal of Instrumentation*, 17(08):P08002, August 2022. URL: <http://dx.doi.org/10.1088/1748-0221/17/08/P08002>, doi:10.1088/1748-0221/17/08/p08002.
49. N. K. Byrnes et al. Fluorescence imaging of individual ions and molecules in pressurized noble gases for barium tagging in  $^{136}\text{Xe}$ . *Nature Commun.*, 15(1):10595, 2024. arXiv:2406.15422, doi:10.1038/s41467-024-54872-0.
50. A. Späth and B. König. Molecular recognition of organic ammonium ions in solution using synthetic receptors. *Beilstein J. Org. Chem.*, page Apr 6;6:32, 2010.
51. Min Shen, Tingting Pan, Yonghao Chen, Juwei Ning, Fengyu Su, and Yanqing Tian. Highly selective fluorescent sensor for ammonium ions. *Sens. Diagn.*, 3(1):79–86, 2024. URL: <http://dx.doi.org/10.1039/D3SD00128H>, doi:10.1039/D3SD00128H.
52. Martin Newcomb, Joseph M. Timko, David M. Walba, and Donald J. Cram. Host-guest complexation. 3. organization of pyridyl binding sites. *J. Am. Chem. Soc.*, 99(19):6392–6398, 1977. doi:10.1021/ja00461a035.
53. Donald J. Cram and Jane M. Cram. Host-guest chemistry. *Science*, 183(4127):803–809, 1974. doi:10.1126/science.183.4127.803.
54. Charles J. Pedersen. Cyclic polyethers and their complexes with metal salts. *J. Am. Chem. Soc.*, 89(26):7017–7036, 1967. doi:10.1021/ja01002a035.
55. Austin G. Seilkop, Amaechi S. Odoh, Nicholas J. Coradi, Jacob I. Wright, Jorge Barroso, and Byoungmoo Kim. Ammonium-binding bifunctional aza-crown ether catalysts for substrate-selective hydroxyl functionalization. *J. Org. Chem.*, 89(18):13338–13344, 2024. doi:10.1021/acs.joc.4c01498.
56. Huiyu Niu, Jie Liu, Helen M. O’Connor, Thorfinnur Gunnlaugsson, Tony D. James, and Hua Zhang. Photoinduced electron transfer (PeT) based fluorescent probes for cellular imaging and disease therapy. *Chemical Society Reviews*, 52(7):2322–2357, 2023. URL: <https://pubs.rsc.org/en/content/articlehtml/2023/cs/d1cs01097b>, doi:10.1039/D1CS01097B.
57. S. Abe et al. Search for Majorana Neutrinos with the Complete KamLAND-Zen Dataset. 6 2024. arXiv:2406.11438.
58. H. Ejiri and S. R. Elliott. Charged current neutrino cross section for solar neutrinos, and background to  $\beta\beta(0\nu)$  experiments. *Phys. Rev. C*, 89(5):055501, 2014. arXiv:1309.7957, doi:10.1103/PhysRevC.

---

[89.055501](#).

59. Benjamin Graham and Laurens van der Maaten. Submanifold sparse convolutional networks. 2017. [arXiv:1706.01307](#).
60. E. Bainglass, B. J. P. Jones, F. W. Foss, M. N. Huda, and D. R. Nygren. Mobility and Clustering of Barium Ions and Dications in High Pressure Xenon Gas. *Phys. Rev.*, A97(6):062509, 2018. [arXiv:1804.01169](#), [doi:10.1103/PhysRevA.97.062509](#).